PASJ: Publ. Astron. Soc. Japan **59**, 419–425, 2007 April 25

Multi-Slit Imaging Spectroscopy Technique: Catalog of Intracluster Planetary Nebulae in the Coma Cluster*

Magda ARNABOLDI
ESO, Karl-Schwarzschild-Str. 2, D-85748 Garching, Germany
and
INAF, Osservatorio Astronomico di Torino, Strada Osservatorio 20, 10025 Pino Torinese, Italy
arnaboldi@to.astro.it
Ortwin GERHARD
Astronomisches Institut, Universität Basel, Venusstrasse 7, CH-4102 Binningen, Switzerland
and
Max-Planck-Institut für extraterrestrische Physik, Giessenbachstrasse, D-85741 Garching, Germany
Sadanori OKAMURA
Department of Astronomy and Research Center for the Early Universe, School of Science, The University of Tokyo, Tokyo 113-0033
Nobunari KASHIKAWA
National Astronomical Observatory of Japan, Mitaka, Tokyo 181-8588
Naoki YASUDA
Institute for Cosmic Ray Research, The University of Tokyo, Kashiwa, Chiba 277-8582
Kenneth C. FREEMAN
R.S.A.A., Mt. Stromlo Observatory, Canberra, 2611 ACT, Australia

(Received 2006 September 23; accepted 2007 January 30)

Abstract

With a new multi-slit imaging spectroscopy (MSIS) technique pioneered at the 8.2 m Subaru telescope and the Faint Object Camera and Spectrograph, we detect and measure the line-of-sight velocities of 40 intracluster planetary nebula candidates associated with the diffuse intracluster population of stars in the Coma cluster core, at nearly 100 Mpc distance. We describe the method for extracting the single two-dimensional spectra from the MSIS image, discuss the criteria for the identification of the emission line objects, and describe the procedure to compute their α, δ (J2000) coordinates. We present the catalog of the intracluster planetary nebula candidates, their spatial location in the surveyed field, and their distribution in the velocity–magnitude plane. Finally, we comment on possible population effects and the use of these planetary nebulae to confirm the distance to the Coma cluster.

Key words: catalog — cosmology: galaxy clusters — ISM: planetary nebulae: general — methods: data analysis — techniques: image processing, spectroscopy

1. Introduction

It is now known that galaxy clusters generally contain an intracluster stellar population which comprises of order 10% of the total cluster light. This population may be observed as diffuse intracluster light (Bernstein et al. 1995; Feldmeier et al. 2002; Zibetti et al. 2005; Mihos et al. 2005), and in nearby clusters also as individual stars (Ferguson et al. 1998; Durrell et al. 2002) or intracluster planetary nebulae (ICPNe: Arnaboldi et al. 2003; Feldmeier et al. 2004; Aguerri et al. 2005 and references therein). ICPNe are the best tracers for dynamical studies of the intracluster light because of their strong [O III] 5007 emission, which allows both their identification and radial velocity measurement (Arnaboldi et al. 2004). When and how the intracluster stellar population originated is a key issue for understanding the evolution of galaxies and galaxy clusters (Napolitano et al. 2003; Murante et al. 2004; Willman et al. 2004; Sommer-Larsen et al. 2005).

We have carried out a pilot survey for ICPNe in the Coma cluster (A 1656), using a multi-slit imaging spectroscopy (MSIS) technique with the Faint Object Camera and Spectrograph (FOCAS) and the Subaru telescope (Gerhard et al. 2005). The technique is similar to the approach used in the search for Lyα emitting galaxies at very high redshifts (Stern & Spinrad 1999; Tran et al. 2004; Martin & Sawicki 2004). We used FOCAS with a mask of parallel multiple slits and a narrow band filter of FWHM 60 Å, centered on the [O III] 5007 Å line at the redshift of the Coma cluster, to obtain spectra of all Planetary Nebulae (PNe) that lie behind the slits.

A total of three mask configurations were observed for a field centered near the peak of the X-ray emission in the Coma cluster core. First detections and the line-of-sight (LOS) velocity distribution from one of the observed mask configurations were presented in Gerhard et al. (2005). We report here the results from the data reduction and analysis of the whole dataset, and present the catalog with positions and magnitudes of the 40 detected PN candidates.

Our observations are described in section 2; the data reduction and identification of the emission line sources

* Based on data collected with the FOCAS spectrograph at the Subaru Telescope, which is operated by the National Astronomical Observatory of Japan, during observing run S04A-024.

Table 1. Observation logbook.

Date	Mask	Total exposure hrs	Average seeing	*BinX* × *BinY*	Number of frames
21.04.04	POS1	6.5	0.″9	3 × 1	12
22.04.04	POS2	6.5	0.″9	3 × 1	13
23.04.04	POS3	3.0	0.″7	2 × 1	6

are outlined in section 3, and the detailed procedure for determining the astrometry of the data sample is presented in section 4. The final catalog of PN candidates from this pilot survey and their spatial, velocity, and magnitude distributions are shown in section 5. Possible population effects in the PN sample and the PN distance to the Coma cluster are briefly discussed in section 6, which is followed by the concluding section 7. Throughout the paper, we use a distance of 95 Mpc $[(m-M)_0 = 34.9]$ for the Coma cluster (Bernstein et al. 1995).

2. Observations

Observations of three masks centered on the field at α (J2000) 12:59:41.784, δ (J2000) 27:53:25.388 were carried out with FOCAS (Kashikawa et al. 2002) at the 8.2 m Subaru telescope (Iye et al. 2004) during the nights of 2004 April 21–23. This field is near the X-ray centroid of the Coma cluster and is essentially coincident with the field observed by Bernstein et al. (1995). The circular FOCAS field of view (FOV) has 6′ diameter (166 kpc at the assumed distance of 95 Mpc). The spatial resolution of FOCAS is 0.″1 pixel^{-1}, so the 6′ diameter corresponds to 3600 pixels.

In our setup, we used grating 300B, which gives a measured dispersion of 1.45 Å pixel^{-1} on the two FOCAS CCD chips. The effective spectral resolution is then $\simeq 7.3$ Å, or 440 km s^{-1}. We also used the *N512* filter with FWHM 60 Å, centered at $\lambda_c = 5121$ Å, the wavelength of the redshifted [O III] emission from a PN at the mean recession velocity of the Coma Cluster (6853 km s^{-1}: Colless & Dunn 1996). The 60 Å FWHM includes only $\pm 1.6 \times \sigma$ the velocity dispersion of galaxies in the Coma core.

The FOCAS circular FOV is imaged onto two CCDs. With the current instrument configuration the dispersion axis is the y-axis on the CCDs, while the spatial direction is along the x-axis. One of the CCDs, chip #1, has an area whose cosmetics is quite poor, with hot columns and pixels which cause the instrument noise to increase significantly and reduces the ability to detect these very faint PN sources.

For a detailed description of the technique and signal-to-noise calculations we refer to Gerhard et al. (2005). A logbook of the observations is given in table 1. Argon–Thorium arc lamp calibration frames were acquired every two exposures; internal flats were also obtained at the beginning and the end of each night. The spectrophotometric standard star was observed through a 5″ wide long slit.

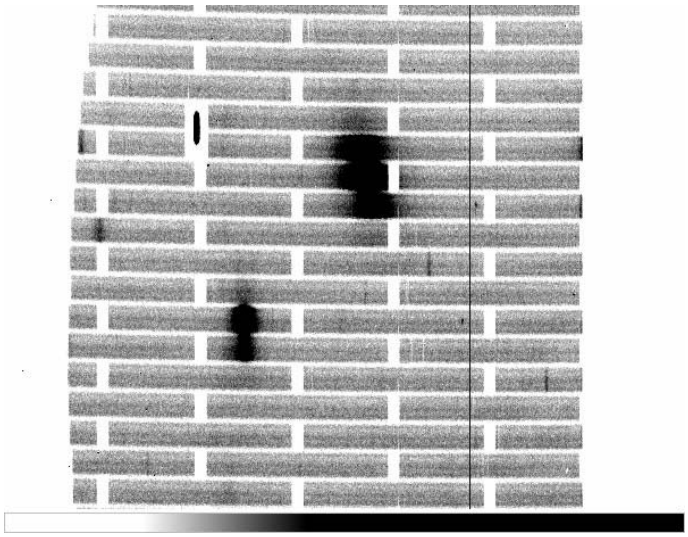

Fig. 1. A section of the medium averaged MSIS image for the mask position POS3. The slitlets are arranged along a total of 70 long slits but with short interruptions for mechanical stability of the mask. Thus the dispersed image of the field resembles a brick wall, made up by adjacent 60 Å wide 2D spectra for which the wavelength direction is along the vertical axis and the spatial direction is along the horizontal axis. The large blobs correspond to galaxies in the field. The continuous spectra from a few stars can also be seen, and near the thin vertical line two of the brighter emission sources are visible.

3. Data Reduction

The complete data reduction of the three masks observed with the MSIS technique is carried out in IRAF, with flux calibration using the spectrophotometric standard star BD +33 2642.

Master biases and flats are produced jointly for the first two nights, and independently for the last night, because of the different binning adopted for the CCD readout. Master flats are normalized by the average counts for the central, best illuminated, stripes. The scientific frames are debiased and flatfielded; before co-addition, bright sharp features are identified in each frame and their rigid offsets in (x, y) are determined with respect to the reference MSIS image, chosen to be the one observed in the best seeing condition during each night. Once the offsets are applied, images are co-added to obtain the median averaged image for the night. The FWHM along the x-axis of point-like continuum sources are then measured in the final median averaged MSIS image and compared with those in the single best frame for each night; the alignment procedure is iterated until the two are comparable. All the frames for a given pointing are median averaged; the final three co-added images for the three pointings are then free of cosmic rays.

A section of the medium averaged MSIS image (chip #2) for the POS3 mask position is shown in figure 1. Each horizontal stripe in figure 1 represents the dispersed image of a 0.″6 slit. The spatial direction is along the horizontal x-axis, while the wavelength direction for each of the 60 Å wide spectra is along the vertical y-axis.

3.1. Identification of Emission-Line Objects

The median averaged MSIS frame for each night is inspected for the presence of emission line objects. Monochromatic, point-like emitters appear as elongated ellipses on the CCD, with a width which depends on the binning adopted for the x-coordinate and seeing (~ 3 pixels for the first and the second nights, and 4 pixels for the third night) and a height of ~ 5 pixels in the wavelength direction.

In these scientific frames we look for the following three kinds of emission line objects:

- unresolved (both in wavelength and in space) emission line objects with no continuum, which are our intracluster planetary nebula (ICPN) candidates;
- continuum point-like sources with unresolved/resolved line emissions. These are most likely background galaxies;
- unresolved line emissions associated with the extended continuum halos of Coma cluster galaxies in the field—such objects are compatible with being PNe associated with the stellar population emitting the continuum light. In this case, a check of the measured LOS velocity is required to confirm the PN candidate-galaxy association.

In total, we detect 60 such emission line objects. Their emission line fluxes are in the range 2.8×10^{-19} to 1.7×10^{-18} erg cm^{-2} s^{-1}; objects with a flux of less than 2.5×10^{-19} erg cm^{-2} s^{-1} are not considered as real. For comparison the noise per pixel in the extracted spectra is 8.5×10^{-20} erg cm^{-2} s^{-1}. The 2D spectra containing the emission line objects are then extracted, rectified, and wavelength calibrated as detailed below.

3.2. Extraction of 2D-Spectra, Calibration, Sky Subtraction, and Wavelength Measurement

The optics of the FOCAS spectrograph produces 2D spectra which are strongly bent, with a curvature which is a function of the x, y position on the chip. Spectra must be rectified before any wavelength calibrations can be carried out. To this aim, we use the arc-lamp exposure taken immediately before or after the reference MSIS image for any given night.

With the task noao.twodspec.apextract.apall, we define a vertical aperture of $\sim$ 45–55 pixel height, centered on the brightest arcline nearest to the position of the identified sources. This brightest arc line is then traced in the arclamp image along the x-axis and a second order Legendre function is interpolated to its curvature. The coefficients of the interpolated Legendre function (which vary across each CCD chip) are stored in a database. Correspondent stripes with height $\sim$ 45–55 pixels are then extracted from both the arclamp and the MSIS image, and saved as rectified individual 2D spectra. Wavelength calibration, using noao.twodspec.longslit.identify and reidentify, and the correction for geometric distortion are computed for the arcline spectrum, using noao.twodspec.longslit.fitcoords, and then applied to the corresponding MSIS science single 2D spectrum.

Once each single MSIS science spectrum is wavelength calibrated and distortion corrected, we subtract the sky background with the IRAF noao.twodspec.longslit.background task. At fixed λ in each single 2D MSIS science spectrum, a third-order Chebyshev function is fitted along the spatial x-coordinate and subtracted off. Because in this step we use a -3, $+2$ sigma clipping algorithm, high frequency structures like point-like sources or the continuum light from Coma galaxies do not affect the fitted function. This step is important to remove any residual modulation in the background caused by the wiggles in the narrow band filter transmission curve.

From the wavelength calibrated, distortion corrected, and sky subtracted MSIS science spectra, we finally measure the wavelength of the redshifted 5007 Å emission line of all PN candidates via a Gaussian fit.

4. Astrometry and Coordinates of Emission-Line Candidates

4.1. Astrometry

At the beginning of each night, an un-dispersed image of each pointing was acquired for the alignment of the MSIS mask. These un-dispersed images can be used to provide the (α, δ) coordinates for the selected emission line objects identified on the MSIS dispersed images.

In what follows, we shall refer to the un-dispersed CCD image of the field as the *Image* plane, and to the dispersed MSIS image of the field as *Spectral* plane. We denote by $(x, y)_{\rm em}$ the (x, y) CCD coordinates of the emission line source in the Spectral plane. In the Spectral plane, we also define as $y_{\rm slit}$ the y-coordinate that the emission source would have if its emission wavelength were $\lambda_{\rm c} = 5121$ Å. Equivalently, this is the y-coordinate of the image centroid of the corresponding slit in $\lambda_{\rm c} = 5121$ Å monochromatic light.

Determining the astrometry for the MSIS catalog of emission line objects then requires the implementation of the following steps:

1. astrometric solution for the Image plane,
2. geometrical transformation from the Spectral to the Image plane, which corrects for the anamorphic distortion[1] caused by the grism. This will also account for the binning adopted in a given night.
3. measurements of the $(x, y)_{\rm em}$, and $y_{\rm slit}$ positions for the emission line candidates in the Spectral plane, thus correcting for the velocity of the emission candidate, and transfer to the Image plane.

These are now described in turn.

Astrometry of the Image plane—We checked the world coordinate system (WCS) of the Image plane with Skycat, by plotting circles at the (α, δ) positions of stars from the USNO catalog. The "default" WCS of the FOCAS frames observed during the nights of our observing run was found not to be correct: all the circles drawn at the correspondent (x, y) Image plane positions of the USNO stars/galaxies' (α, δ) are systematically offset from the objects on the FOCAS image. A new WCS is thus computed, for each CCD chip independently, using images.imcoords.ccmap and a second order polynomial.

[1] Anamorphic distortion: a type of distortion in which the spatial magnification varies between the different directions.

Geometrical transformation from Image to Spectral plane—For a given night, the reference stars and galaxies are identified both in the Image and Spectral plane. For each reference star or galaxy, we determine $y_{\rm slit}$ as the center of its 60 Å spectrum along the y-axis. For the low spectral resolution of our MSIS images, the small variation of the filter bandpass across the field can be neglected to within the accuracy of the other steps. Then we build a matrix which lists the $(x, y)_{\rm Image}$, $(x, y)_{\rm Spectral}$ where

- $(x, y)_{\rm Image}$ corresponds to the centroid of the light distribution of a given object in the Image plane,
- $x_{\rm Spectral}$ corresponds to the center of the x-FWHM of the stellar spectrum,
- $y_{\rm Spectral}$ is the center of the 60 Å wide continuous spectrum of the star.

This matrix is used to compute the geometrical transformation from the Spectral to the Image plane, with immatch.geomap, and corrects for the anamorphic distortion caused by the grism.

Measurement of the $(x, y)_{\rm em}$ *and* $y_{\rm slit}$ *in the Spectral plane for the emission line candidates*—For each emission line object, we measure its coordinates $(x, y)_{\rm em}$ in the Spectral plane. From the $y_{\rm em}$ we obtain the object's slit centroid position on the Spectral plane, $y_{\rm slit}$, which to first-order approximation equals

$$y_{\rm slit} = y_{\rm em} - (\lambda_{\rm obs} - \lambda_{\rm c})/1.45, \quad (1)$$

where $\lambda_{\rm c} = 5121$ Å. Therefore, from the measured $(x, y)_{\rm em}$, $\lambda_{\rm obs}$ we compute the $(x_{\rm em}, y_{\rm slit})_{\rm Spectral}$ pairs.

Computing (α, δ) *J2000 for the emission line candidates*—The $(x_{\rm em}, y_{\rm slit})_{\rm Spectral}$ pairs are now mapped in $(x_{\rm em}, y_{\rm slit})_{\rm Image}$ via the geometrical transformation. Once the WCS is applied to $(x_{\rm em}, y_{\rm slit})_{\rm Image}$ we get the correspondent (α, δ) J2000 coordinates of the emission line sources. In table 2, we list the (α, δ) for our ICPN candidates in the USNO coordinate system.

4.2. Error Budget for the Final Catalog

Because emission line sources are identified and their positions measured on the Spectral plane, the accuracy of this astrometric solution will be worse than the one usually achieved in the standard imaging mode, given the FOCAS pixel angular resolution and the accuracy of the USNO star catalog. The total error budget for the astrometry of the ICPN catalog comprises the following contributions:

1. Slit width—The slit is 0.″8 wide, so each $y_{\rm slit}$ has an absolute error[2] of $\sim \pm 0.''2$. So $(0.''2)^2$ should be added in quadrature to the y-rms error.
2. Astrometry of the Image plane—The FOCAS-WCS step had the following rms error: $(0.''6, 0.''8)$ in RA and DEC respectively for chip #1, and $(1.''5, 0.''7)$ similarly for chip #2. The relatively large error in this part is probably caused by having to use extended sources (galaxies) to define the transformation adequately.
3. Geometrical transformation from Spectral to Image plane—The average rms errors for the geometrical transformation from Image to Spectral plane are $(0.''9, 0.''6)$ in $(x, y)_{\rm Image}$ for both CCD chips. This step could be made more accurate if an un-dispersed arclamp image through the mask or through a pin-hole mask were available, but we see that it does not dominate the errors here.

The final catalog has rms errors in RA (along y), and DEC

[2] If the source position is offset from the slit center by a half the slit width, half of the light is lost; for the large majority of our sources, the emission could then no longer be detected. So we take 1/4 of a slit width as their typical displacement.

Table 2. ICPN candidates in the Coma FOCAS fields.

ID	α(J2000)	δ(J2000)	$\lambda_{\rm obs}$ nm	m_{5007}
Chip #2				
IPN 201	12:59:35.22	27:54:12.3	510.6	30.4
IPN 202	12:59:42.89	27:54:06.0	510.9	30.7
IPN 203	12:59:44.75	27:53:59.8	510.6	30.7
IPN 204	12:59:39.35	27:55:59.5	513.3	31.3
IPN 205	12:59:49.24	27:55:39.0	512.9	31.4
IPN 206	12:59:49.63	27:53:28.8	511.5	31.9
IPN 207	12:59:54.14	27:54:09.1	512.3	31.9
IPN 208	12:59:37.95	27:56:08.7	511.0	32.1
IPN 209	12:59:45.91	27:55:29.7	511.8	32.1
IPN 210	12:59:40.49	27:56:02.5	510.5	32.2
IPN 211	12:59:46.50	27:56:18.2	513.8	32.3
IPN 212	12:59:29.01	27:53:33.2	513.1	32.3
IPN 213	12:59:35.76	27:53:32.9	511.8	32.4
IPN 214	12:59:47.33	27:54:58.8	511.4	32.4
IPN 215	12:59:43.51	27:55:21.7	509.0	32.5
IPN 216	12:59:49.33	27:55:01.7	513.0	32.6
IPN 217*	12:59:43.42	27:54:20.5	511.3	32.6
IPN 218	12:59:48.71	27:53:31.8	509.6	32.6
IPN 219	12:59:44.29	27:53:38.5	508.8	32.6
IPN 220	12:59:50.45	27:55:46.1	508.7	32.6
IPN 221	12:59:48.64	27:55:44.7	511.9	32.7
IPN 222	12:59:33.60	27:54:55.6	511.0	32.7
IPN 223	12:59:45.65	27:54:43.5	511.7	32.7
IPN 224*	12:59:43.75	27:54:52.0	511.4	32.8
IPN 225	12:59:32.52	27:55:17.6	510.5	32.8
IPN 226	12:59:50.49	27:54:20.8	512.2	32.8
Chip #1				
IPN 101	12:59:38.38	27:50:56.7	511.4	31.8
IPN 102	12:59:28.82	27:52:55.3	511.6	31.9
IPN 103	12:59:31.95	27:51:25.5	510.1	31.9
IPN 104*	12:59:45.06	27:50:54.4	514.9	32.2
IPN 105	12:59:41.42	27:50:42.4	509.7	32.3
IPN 106	12:59:51.98	27:51:37.7	509.4	32.3
IPN 107	12:59:33.62	27:51:21.6	508.9	32.3
IPN 108	12:59:49.37	27:51:09.9	512.0	32.5
IPN 109	12:59:36.22	27:53:14.8	511.7	32.7
IPN 110	12:59:38.58	27:51:27.0	510.9	32.7
IPN 111	12:59:50.68	27:51:51.2	508.7	32.7
IPN 112	12:59:53.79	27:51:59.5	511.3	32.8
IPN 113	12:59:32.43	27:51:47.4	511.9	32.9
IPN 114	12:59:45.37	27:51:25.2	511.4	32.9

* They may be bound to nearby Coma galaxies.

(along x) of ($0\farcs9, 1\farcs2$) for chip #1 and ($1\farcs6, 1\farcs4$) for chip #2. These are computed by adding the variances, assuming Gaussian-distributed errors. Due to the large rms in both right ascension and declination for the final catalog, a possible spectroscopic follow-up for individual candidates would best be carried out with an IFU.

5. Flux Measurements and Magnitudes for the PN Candidates

The integrated flux from the [O III] line of a PN is usually expressed in a "m_{5007}" magnitude using the definition first introduced by Jacoby (1989),

$$m(5007) = -2.5 \log F_{5007} - 13.74, \quad (2)$$

which gives the PN luminosity in equivalent V magnitude when F_{5007} is the total [O III] 5007 flux in erg cm^{-2} s^{-1} of the PN. From the integrated flux in the detected 5007 Å line and the spectroscopic standard star calibration, we derive a measurement of the m_{5007} magnitude for all the PN candidates.

However, because MSIS is a blind search technique, the detected emission line objects may not be centred on the slitlets, and hence their measured fluxes are systematically underestimated due to slit loss effects. For example, an apparently faint PN may be an intrinsically bright PN with a large offset from the slit center (and a significant slit loss), or may indeed be an intrinsically faint PN correctly aligned with the slit. Thus *individual* m_{5007} magnitudes based on the measured fluxes in MSIS have systematic errors which cannot be corrected; only the luminosity function for a PN *population* could be corrected for these errors in a statistical sense. The statistical determination of the planetary nebula luminosity function (PNLF) for distance determination is beyond the scope of the current paper; the main goal here is to develop and test an observing technique and corresponding data analysis which can detect the [O III] 5007 Å emission of PNe at 100 Mpc distance, and measure their line-of-sight velocities and positions. Thus we only give a simple estimate of the errors in the m_{5007} magnitudes from the sky noise per pixel and from the slit losses.

- The sky noise per pixel translates to an error of 0.05 mag for the brightest PN candidates, and to 0.3 mag for the faintest.
- As the typical displacement of a source in the slit we take one quarter of the slit width. In this case the fraction of light lost, assuming a seeing FWHM equal to the slit angular width, amounts to 18%, i.e. 0.2 mag. As stated already in section 4, if the source position is offset from the slit center by half a slit width, half of the light is lost, and the majority of our current sources could no longer be detected.

Thus in the first magnitude interval of the PNLF, the estimated error for the magnitudes measured with the MSIS technique is ~ 0.2 mag, and ~ 0.4 mag at the faint end.

6. Catalog of Planetary Nebula Candidates in the MSIS field and Their Spatial Distribution

Based on the criteria described in subsection 3.1, the 60 emission line objects detected in the three MSIS masks in our field in the Coma cluster core can be classified as follows:

- 35 PN candidates are ICPNe, with no continuum flux;
- 20 are background galaxies;
- 5 are PN candidates projected against the extended continuum halos of nearby Coma galaxies.

The classification of the last group of candidates can be further checked by comparison with the LOS velocities of Coma galaxies in the FOCAS field. The results from this analysis (Gerhard et al. 2007) show that two of the five candidates may be bound to nearby Coma galaxies, while the other three have large velocity differences with respect to their nearby galaxies, so are reclassified as ICPNe. In addition, one of the 35 ICPN candidates is sufficiently close in position and velocity to a Coma galaxy that it is reclassified as a galaxy PN.

The evidence that the emission objects detected in our study are indeed PNe is as follows. (i) They are unresolved both spatially and in wavelength, as described in Gerhard et al. (2005). (ii) They have no detectable continuum, to a limit of 1.6×10^{-20} erg s^{-1} cm^{-2} Å^{-1}. (iii) We have seen both lines of the [O III] doublet in all four sources with sufficient flux in the [O III] 5007 Å line and at sufficiently large recession velocity $v_{\rm obs} > 7400$ km s^{-1} that also $\lambda 4959$ Å is redshifted into the wavelength range probed. (iv) The emission fluxes of the brightest objects are consistent with those of the brightest PNe in a population at distance 100 Mpc. (v) The distribution of recession velocities is centered around the Coma cluster and is inconsistent with a population of background objects uniformly distributed in velocity.

The α, δ (J2000) coordinates, the observed wavelength of

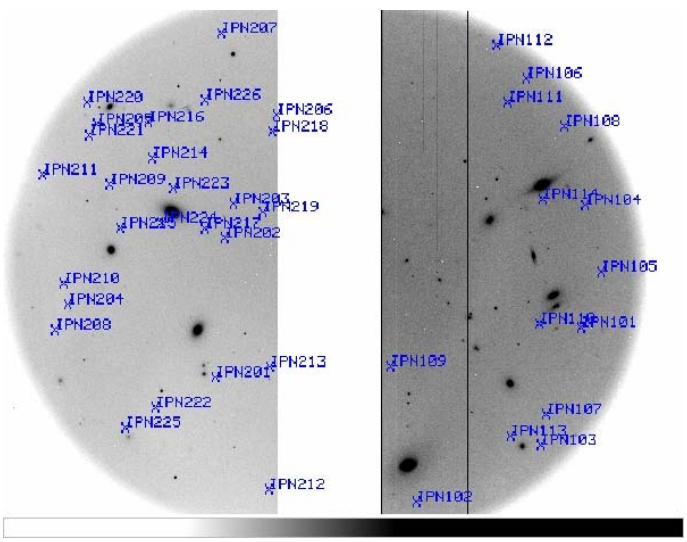

Fig. 2. The spatial distribution of all PN candidates in the FOCAS FOV centered near the X-ray peak in the Coma cluster. North is to the left, and East is up.

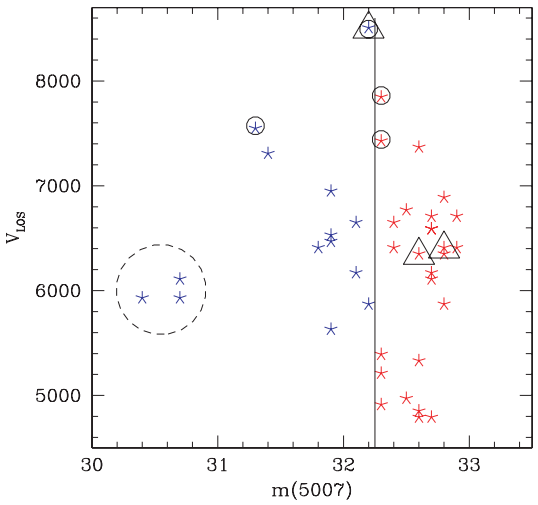

Fig. 3. Observed radial velocities of the 40 PN candidates in the Coma core vs. their m_{5007} magnitudes. The "bright" sample includes PNe brighter than 32.25 mag, the "faint" sample includes PNe fainter than this limit. The "bright" and "faint" samples have average velocities of $\bar{v} = 6424$ km s^{-1} and $\bar{v} = 6131$ km s^{-1} respectively, but the bright sample has smaller standard deviation (575 km s^{-1}—the galactic IPN 104 not included) than the fainter sample (905 km s^{-1}). The PNe indicated by triangles are those possibly bound to Coma galaxies, and the circled PNe have detected 4959 Å emission in addition to the brighter 5007 Å emission. The brightest candidates are enclosed in the plot by a dashed circle. For the continuum flux limit given, their equivalent widths are EW > 110 Å, sufficient to rule out compact H II regions such as or brighter than those observed in Virgo (Gerhard et al. 2002).

the line emission, and the m_{5007} magnitudes for the 40 PN candidates are given in table 2. The four sources with ID in boldface are those for which also the 4959 Å line is detected. The starred objects IPN 217, 224, and 104 may be bound to nearby Coma galaxies. The distribution of these PN candidates in the FOCAS field are shown in figure 2, and their distribution in the velocity–magnitude plane is shown in figure 3.

7. Discussion

7.1. *Are There Population Effects in the Coma PNe Sample?*

In the plot of LOS velocities vs. m_{5007} magnitudes for the Coma PN in figure 3, we adopt $m^*_{5007} = 32.25$ [3] as a separation between a bright and a faint PN subsample. The LOS velocity distributions of these two subsamples indeed show some differences. The LOS velocity distribution of the faint PNe is strongly bimodal, with an over-density at ~ 5000 km s^{-1} and a second over-density at ~ 6500 km s^{-1}. The velocities of the bright PNe follow a single-peaked, broader distribution centred at 6424 km s^{-1} and with $\sigma = 575$ km s^{-1}.[4] A Kolmogorov–Smirnov test between the velocity distributions of the bright and faint PN subsamples indicates a moderate probability (28%) for the PN bright sample to be drawn from the faint one. Thus these samples are only marginally different; the number of PNe is too small to be sure.

If this difference is confirmed with a larger PN sample, it could not be explained by instrumental or cluster depth effects, but would have to be an intrinsic population property. The slit loss effects do not change the velocity distribution, and if we take 1 Mpc as a typical "size" for the Coma core, and a cluster distance 100 Mpc, then the magnitude difference between a PN placed at the "front edge" of the cluster core and those placed at the "back end" would be 0.02 mag, negligible compared to the magnitude spread in figure 3. A correlation between PN magnitudes and their observed dynamics has been detected previously in the elliptical galaxy NGC 4697 (Sambhus et al. 2006).

Recent theoretical work now supports distinct post AGB evolutionary channels for PNe at the bright cut-off of the PN luminosity function (PNLF) and those at fainter magnitudes. While Marigo et al. (2004) pointed towards different ages in the parent stellar population, and required the presence of an intermediate age population in early-type galaxies to ensure invariance of the PNLF across Hubble morphological types, Ciardullo et al. (2005) pointed towards the evolution of blue stragglers and coalescing binary stars as the progenitors of the PN at the PNLF bright cut-off. The recent work by Buzzoni et al. (2006) rediscussed the single star evolution channel in the post-AGB and subsequent PN phases, and concluded that a dimming of the PNLF in old and metal-rich stellar populations is to be expected. In the diffuse light in galaxy clusters these PN populations can be segregated in phase-space, given that the dynamical time-scales are significantly longer than in galaxies. This could be the cause for the LOS velocity vs. magnitude distribution observed for the PN sample in the Coma core.

7.2. *The Distance to Coma from PNe*

The planetary nebula luminosity function (PNLF) is an important tool for extragalactic distance scale (Jacoby 1989; Jacoby et al. 1992; see Ciardullo 2005 for a recent review.) The brightest candidate in table 2 has $m = 30.4$. If we assume that this candidate is centered in its slit and corresponds to the absolute magnitude of the PNLF cut-off ($M_* = -4.48$) observed in nearby galaxies (Jacoby et al. 1989), we obtain a nominal distance modulus of $(m - M)_0 = 34.9$. Although the coincidence with our assumed value is accidental, this gives support for the overall usefulness of the planetary nebula luminosity function as a distance tool.

8. Summary and Conclusion

The detection of PNe in the Coma Cluster at a distance of $\simeq 95$ Mpc (Bernstein et al. 1995) requires measuring fluxes of 2.2×10^{-18} erg s^{-1}cm^{-2} (Ciardullo et al. 2002) or fainter. This was successfully achieved by Gerhard et al. (2005) using a technique that is similar to the approach used in the search for Lyα-emitting galaxies at very high redshift. It combines a mask of parallel multiple slits with a narrow band filter, centered around the [O III] 5007 line at the redshift of the Coma Cluster, to obtain spectra of all PNe that happen to lie behind the slits. Because the [O III] emission lines from PNe are only ~ 20 km s^{-1} wide (Phillips 2002), their entire flux

[3] This corresponds to 8 ADU or 4×10^{-19} erg cm^{-2} s^{-1}.

[4] The main Coma cluster is at $v_{\rm sys} = 6853$ km s^{-1} and $\sigma = 1082$ km s^{-1} (Colless & Dunn 1996).

still falls into a small number of pixels in the two-dimensional spectrum, determined by the slit width and seeing. On the contrary, the sky emission is dispersed in wavelength, allowing a large increase in the signal-to-noise ratio (S/N). The narrow band filter limits the length of the spectra on the CCD, so that more slits can be exposed. For brevity, we refer to this as the multi-slit imaging spectroscopy (MSIS) technique. No conventional imaging technique can decrease the sky surface brightness in a similar way.

In this paper we have described in detail the procedure for the data reduction of the MSIS images and the astrometry of the detected emission line objects. The catalog of the detected PN candidates is presented with (α, δ) coordinates, $\lambda_{\rm obs}$, and m_{5007}.

We note that the PNe detected with the MSIS technique in the Coma cluster core at $\simeq 100$ Mpc distance represent the most distant individual stellar objects ever detected, but for the high-z supernovae. The MSIS technique will allow us to extend distance measurements with the PNLF to galaxy clusters out to ~ 100 Mpc distance, and to use the radial velocities of these PNe to study the kinematics of the intracluster light and the evolution of the galaxy populations in these clusters.

We acknowledge financial support by the Swiss SNF and by INAF. This work is supported in part by Grant-in-Aid (No.16540212) from Ministry of Education, Culture, Sports, Science and Technology of Japan. We are grateful to the on-site Subaru staff for their support.

References

Aguerri, J. A. L., Gerhand, O. E., Arnaboldi, M., Napolitano, N. R., Castro-Rodriguez, N., & Freeman, K. C. 2005, AJ, 129, 2585
Arnaboldi, M., et al. 2003, AJ, 125, 514
Arnaboldi, M., Gerhard, O., Aguerri, J. A. L., Freeman, K. C., Napolitano, N. R., Okamura, S., & Yasuda, N. 2004, ApJ, 614, L33
Bernstein, G. M., Nichol, R. C., Tyson, J. A., Ulmer, M. P., & Wittman, D. 1995, AJ, 110, 1507
Buzzoni, A., Arnaboldi, M., & Corradi, R. L. M. 2006, MNRAS, 368, 877
Ciardullo, R. 2005, in International Conference on Planetary Nebulae as Astronomical Tools, AIP Conf. Proc., 804, 277
Ciardullo, R., Feldmeier, J. J., Jacoby, G. H., Kuzio de Naray, R., Laychak, M. B., & Durrell, P. R. 2002, ApJ, 577, 31
Ciardullo, R., Sigurdsson, S., Feldmeier, J. J., & Jacoby, G. H. 2005, ApJ, 629, 499
Colless, M., & Dunn, A. M. 1996, ApJ, 458, 435
Durrell, P. R., Ciardullo, R., Feldmeier, J. J., Jacoby, G. H., & Sigurdsson, S. 2002, ApJ, 570, 119
Feldmeier, J. J., Ciardullo, R., Jacoby, G. H., & Durrell, P. 2004, ApJ, 615, 196
Feldmeier, J. J., Mihos, J. C., Morrison, H. L., Rodney, S. A., & Harding, P. 2002, ApJ, 575, 779
Ferguson, H. C., Tanvir, N. R., & von Hippel, T. 1998, Nature, 391, 461
Gerhard, O., Arnaboldi, M., Freeman, K. C., & Okamura, S. 2002, ApJ, 580, L121
Gerhard, O., Arnaboldi, M., Freeman, K. C., Kashikawa, N., Okamura, S., & Yasuda, N. 2005, ApJ, 621, L93
Gerhard, O. E., et al. 2007, A&A in press (astro-ph/0703770)
Iye, M., et al. 2004, PASJ, 56, 381
Jacoby, G. H. 1989, ApJ, 339, 39
Jacoby, G. H., et al. 1992, PASP, 104, 599
Jacoby, G. H., Ciardullo, R., Booth, J., & Ford, H. C. 1989, ApJ, 344, 704
Kashikawa, N., et al. 2002, PASJ, 54, 819
Marigo, P., Girardi, L., Weiss, A., Groenewegen, M. A. T., & Chiosi, C. 2004, A&A, 423, 995
Martin, C. L., & Sawicki, M. 2004, ApJ, 603, 414
Mihos, J. C., Harding, P., Feldmeier, J., & Morrison, H. 2005, ApJ, 631, L41
Murante, G., et al. 2004, ApJ, 607, L83
Napolitano, N. R., et al. 2003, ApJ, 594, 172
Phillips, J. P. 2002, A&A, 393, 1027
Sambhus, N., Gerhard, O., & Méndez, R. H. 2006, AJ, 131, 837
Sommer-Larsen, J., Romeo, A. D., & Portinari, L. 2005, MNRAS, 357, 478
Stern, D., & Spinrad, H. 1999, PASP, 111, 1475
Tran K.-V., Lilly, S. J., Crampton, D., & Brodwin, M. 2004, ApJ, 612, L89
Willman, B., Gorernato, F., Wadsley, J., & Quinn, T. 2004, MNRAS, 355, 159
Zibetti, S., White, S. D. M., Schneider, D. M., & Brinkmann, J. 2005, MNRAS, 358, 949